Origin, structure and exposure history of a wave-cut platform more than 1 Ma in age at the coast of northern Spain: a multiple cosmogenic nuclide approach

J. Alvarez-Marrón [a,*], R. Hetzel [b], S. Niedermann [c], R. Menéndez [d], J. Marquínez [d]

[a] *Institute of Earth Sciences, CSIC, c/ Lluis Sole i Sabaris s/n, E-08028 Barcelona, Spain*

[b] *Geologisch-Paläontologisches Institut, Westfälische Wilhelms-Universität Münster, Corrensstr. 24, D-48149 Münster, Germany*

[c] *GeoForschungsZentrum Potsdam, Telegrafenberg, D-14473 Potsdam, Germany*

[d] *INDUROT, Campus de Mieres, University of Oviedo, E-33005 Oviedo, Asturias, Spain*

Abstract

Along the Asturian coast of northern Spain an uplifted wave-cut platform extends for ~100 km east-west. The steep cliff which bounds the gently seaward-dipping platform to the north increases in height from 30 m in the west to 100 m in the east and reflects the overall eastward increase in platform elevation. The southern edge of the 2–4-km-wide platform runs along the foothills of the Cantabrian Mountains, as constrained by a high-resolution digital elevation model. The marine platform, which was carved into deformed Paleozoic bedrock with abundant quartzite beds, is largely covered by weathered marine and continental sediments. Quartzite samples from flat bedrock outcrops which are currently not covered by sediment or soil yield cosmogenic nuclide concentrations (^{21}Ne, ^{10}Be and ^{26}Al) that demonstrate a long and complex exposure history, including periods of burial with partial or complete shielding from cosmic rays. The combination of multiple cosmogenic nuclides yields a *minimum* age of 1-2 Ma for the platform. Taking into account (i) the horizontal and vertical extent of the platform, (ii) the high resistance to erosion of the quartzitic bedrock, and (iii) published data on the magnitude of past sea level fluctuations, we suggest that the wave-cut platform formed in the Pliocene. Subvertical faults cutting the platform at high angles to the coastline offset the southern edge of the platform by 20 to 40 m and reactivate the pre-

existing anisotropy in the Paleozoic bedrock. Uplift and crustal deformation of the coastal region have occurred after platform formation in the Pliocene and may still be active. The slow deformation of the northern edge of the Iberian plate including the Cantabrian Mountains may result from the ongoing slow convergence at an incipient subduction zone extending along the coast of northern Spain.

Keywords: Marine terrace; Wave-cut platform; Cosmogenic nuclides; Pliocene; Slow uplift; Slow convergence; Northern Spain

* Corresponding author. Tel.: + 34 93 409 54 10; Fax: + 34 93 411 00 12; E-mail address: jalvarez@ija.csic.es

1. Introduction

Marine terraces form through the interaction of uplifting coastal regions and rapid sea-level oscillations (e.g. Burbank and Anderson, 2001). Whenever the sea level remains at approximately the same relative position with respect to a landmass, continued wave attack forms a planar abrasion surface or wave-cut platform by driving a sea cliff landward (Figure 1) (e.g. Bradley and Griggs, 1976; Anderson et al., 1999). When the sea level declines, the actively eroding platform is abandoned, leaving behind a planar bedrock surface with very low relief that dips 1-3º seaward and may be thinly mantled by marine or beach deposits. If, by the time the sea level reaches a subsequent highstand, the landmass has risen sufficiently, the old platform will be preserved and a new platform will be etched into the landmass at a lower elevation (e.g. Anderson et al., 1999). Typically, wave-cut platforms that have formed during Pleistocene sea-level highstands are 100-500 m wide, depending on the resistance to erosion of the underlying bedrock. For broader platforms to form, a repeated re-occupation of a platform by the sea during successive highstands appears to be the only feasible mechanism (e.g. Kelsey and Bockheim, 1994; Burbank and Anderson, 2001).

Owing to their planar geometry and lateral extent, marine terraces are excellent geomorphic markers that have been widely used in the past to quantify rates of rock uplift (e.g. Merritts and Bull, 1989; Kelsey and Bockheim, 1994; Chappell et al., 1996; O'Neal and McGeary, 2002). In particular, the landward edge of marine terraces – called shoreline angle (Figure 1) – is an important geomorphic feature, because it provides a linear paleohorizontal marker that allows to determine spatial variations in the amount of uplift and the tilting of crustal blocks (e.g. Kelsey and Bockheim, 1994; Burbank and Anderson, 2001). Marine terraces have also been used to quantify the differential rock uplift due to faulting (Kelsey and Bockheim, 1994; Hsieh et al., 2004; Marquardt et al., 2004) and fold growth (Grant et al., 1999). It is striking that previous studies have mainly concentrated on Late Pleistocene uplift processes, while studies that use marine terraces to tackle longer-term processes of coastal uplift are scarce (e.g. Westaway et al., 2006); probably because terraces are erased with time (Anderson et al., 1999). In this study, we use a digital elevation model to infer long-term displacements on poorly exposed faults which offset the paleoshoreline angle of a marine terrace.

In order to determine rock uplift rates from marine terraces, a precise determination of their age of emergence above sea level is necessary. One technique that offers this possibility is surface exposure dating. This method is based on measuring concentrations of cosmogenic nuclides, which are continuously produced by the interactions of cosmic rays with rock at the Earth's surface (e.g. Lal, 1991). Cosmogenic nuclides commonly applied in exposure dating include ^{3}He, ^{10}Be, ^{21}Ne, ^{26}Al, and ^{36}Cl (e.g. Lal, 1991; Gosse and Phillips, 2001; Niedermann, 2002). The use of a particular nuclide depends on the rock type and age range to be dated. In particular, a stable nuclide such as ^{21}Ne offers the advantage of investigating exposure histories longer than a few million years (Niedermann, 2002). Very few previous studies have applied surface exposure dating to marine terraces and all of them have dealt with terraces

younger than ~250 ka. Stone et al. (1996) determined the age of the main rock platform in western Scotland with ^{36}Cl as Younger Dryas, whereas Kim and Sutherland (2004) used ^{10}Be and ^{26}Al to demonstrate that the lowest of several bedrock terraces at the coast of New Zealand formed during the last interglacial ~125 ka ago. A third study applied depth profiles of ^{10}Be in beach deposits to date a flight of marine terraces in California (Perg et al., 2001). However, none of these investigations combined the cosmogenic nuclides ^{10}Be, ^{26}Al, and ^{21}Ne. Our study sheds new light on the geomorphological and tectonic history of a very broad and unusually old marine terrace by applying several cosmogenic nuclides. Using the stable nuclide ^{21}Ne and the two radioactive nuclides ^{10}Be and ^{26}Al we demonstrate that after generation of the wave-cut platform in the Pliocene long periods of burial must have occurred. Nevertheless, the planar shape of the surface is still largely preserved, suggesting that such geomorphic features may survive over millions of years even under humid climate conditions.

2. Regional geological and geomorphological background

Along the entire coast of northern Spain (Figure 2A), several erosional surfaces – interpreted to be of marine origin – have previously been described (Flor, 1983; Mary, 1983; Mary, 1985; Moñino et al., 1988; Marquinez, 1992). Mary (1983) inferred a Miocene-Pliocene age for several "planation" surfaces that occur in the Asturias region between 60 and 260 m above sea level. This age interpretation is mainly based on geometric relationships with the structure of the substratum, the degree of alteration in weathering mantles, and correlation to known transgressions over the continental margin of northern Spain (Mary, 1983). South of the Asturian coastline, the Cantabrian Mountains rise abruptly from the coast to more than 2500 m over a distance of 50-70 km (Figure 2B). Rivers on the northern slope of the Cantabrian Mountains are deeply incised into the bedrock and have steep valley slopes

(Fernandez et al., 1997). The mountains are underlain by a deformed Paleozoic basement (Julivert, 1987; Pérez-Estaún et al., 1990, 1991) that was uplifted during Alpine times in the western prolongation of the Pyrenees (Alonso et al., 1996; Pulgar et al., 1996).

In western Asturias a single, low-relief surface appears above a sea cliff between the Peñas Cape and the Ribadeo estuary and extends to the foothills of the Cantabrian Mountains (Figures 2B, 2C). Previous studies, i.e. Mary (1983) and references therein, agreed on the marine origin of this surface based on: (1) the very low seaward dip of the surface, (2) the size and morphology of clasts contained in gravel deposits that fill local bedrock depressions, and (3) the presence of marine shells at one site on the Peñas Cape (Mary, 1983). The detailed study by Mary (1983) includes a compilation of all available data and concludes that the surface corresponds to a single erosion surface that formed during a marine transgression, presumably in the Pliocene. We further refer to the wave-cut platform and its sedimentary cover as marine terrace. The Variscan bedrock into which the wave-cut platform has been eroded is relatively uniform with respect to its strength and mainly composed of very resistant lithologies such as quartzites interbedded with minor amounts of slates. The foliation and bedding in the Variscan bedrock dip rather steeply and trend at high angles to the shoreline (Figure 2C).

3. Morphology and structure of the marine terrace

The morphology of a single terrace that appears in a 100-km-long reach of the Asturian coast, between the Peñas Cape and the Ribadeo estuary, has been analyzed using a digital elevation model (DEM) with a horizontal resolution of 10 m (Figure 3A). The error in the vertical component of the DEM is ±2.4 m, as derived from the comparison of a 4 km^2 portion of the DEM with a high-precision LIDAR (Laser Imaging Detection And Ranging) system. The DEM shows a single, low relief surface, bounded by steep mountain slopes on the inland side

that terminates against a vertical cliff on the sea side between the Ribadeo and Nalón estuaries (Figure 2C). Several rivers have deeply incised the low relief surface and the larger ones form estuaries.

Those areas of the marine terrace that are best preserved and have very low slopes have been visualized by construction of a SLOPE model from the DEM. The SLOPE model identifies a single, low relief surface between the estuaries of Ribadeo and Nalón (Figure 3B). Its width decreases eastward from about 4 to 2 km, extending from the sea cliff to the foot of the Cantabrian Mountains. This continuous surface corresponds to the marine terrace previously identified by Mary (1983). Importantly, the DEM documents a progressive lowering of the surface from east to west that is also reflected in the height of the sea cliff, which is 100 m near the Nalón estuary in the east but only about 30 m in the west (Figures 3, 4). Near the Avilés estuary, where Mary (1983) described three "planation levels", the DEM and the SLOPE models show a much wider zone with discontinuous low-slope surfaces at topographic highs with different elevations. The morphological change from a single continuous surface to this more complex topography coincides with a change in the dominant lithologies of the bedrock that occurs at a major fault, the Narcea thrust, which separates resistant metasediments in the west from soft sedimentary rocks (mainly shales, marls, limestones, and sandstones) in the east (Figure 5A). In contrast to Mary (1983), we interpret the complex topography of this region to have formed from a single erosion surface, which was subsequently modified by faulting and erosion.

The SLOPE model is remarkably useful in defining the location of the single paleoshoreline angle, i.e. the junction between the edge of the abrasion platform and the steeper mountain slopes (Figures 3B, 4, 5A). Identifying the paleoshoreline angle is important because it provides a reference horizontal datum that allows us to determine spatial variations in the amount of rock uplift due to faulting and tilting of crustal blocks. Although the

identified paleoshoreline angle is subhorizontal along most of its length, its elevation changes abruptly where it is offset by faults with NE and NW azimuths (Figure 5A). The throw on these faults has been determined from the vertical offset of the paleoshoreline angle on adjacent fault blocks as observed in the SLOPE model. The NE-trending faults coincide with the trend of the main basement structures of Variscan age. The faults appear to have caused tilting of the fault-bounded blocks as shown by the variable dip directions of the marine terrace calculated from the DEM in the different blocks. Across most faults the vertical offset of the paleoshoreline angle is 20 to 40 m, although larger throws occur near the Narcea Thrust (Figure 5A). For instance, west of the Nalón estuary the paleoshoreline angle is displaced vertically by ~120 m. It is important to note that the DEM cannot resolve faults that displace the paleoshoreline angle by less than 5 m, or those whose scarp is covered by sediments. For instance, a strike-slip fault with a throw of 2 m is exposed SSE of Cape Busto along a main road, but fault-related sediments and colluvium cover the scarp (Figure 5B). Southwest of Cape Busto the paleoshoreline angle increases in elevation by 20 m over a distance of 1.5 km (Figure 5A). This feature and the converging dip directions of the marine terrace to the west of the cape may indicate an open synform, which folds the terrace. Overall the elevation of the paleoshoreline angle increases from 100 m in the west to 220 m in the east.

From the different faults mapped here, only the NW-trending fault south of Cape Busto is shown on regional geological maps. According to Alonso et al. (1991), this fault displaces structures in the basement and has therefore a post-Variscan age. The other faults – described here for the first time – displace the paleoshoreline angle of the marine terrace and have therefore been active after the generation of the wave-cut platform.

4. Surface exposure dating

4.1 Introduction to theory

Nuclear interactions of cosmic rays with terrestrial surface matter produce a large number of different cosmogenic nuclides, but only a few of them can be detected in rocks because they are very rare or even absent otherwise. Among them are the stable noble gas isotope ^{21}Ne and the radioactive nuclides ^{10}Be and ^{26}Al, with half-lives of 1.5 and 0.7 Ma, respectively (e.g. Gosse and Phillips, 2001; Niedermann, 2002). The production rates of the different cosmogenic nuclides depend on the chemical composition of the rock or mineral and vary with latitude and elevation (e.g., Lal, 1991; Dunai, 2000). It is thus necessary to scale the production rates, usually given for sea level and high latitudes (>60°), to the sampling locations. Using the site-specific production rate, the measured concentration of a cosmogenic nuclide can be converted into an exposure age for geomorphic surfaces that have not been eroded or shielded. If erosion has removed material from the original surface or if that surface was temporarily covered, the calculated exposure age will underestimate the true age of the surface. As a consequence, exposure ages based on a single cosmogenic nuclide must be considered as minimum ages, unless the lack of erosion or burial can be demonstrated.

In principle, it is possible to determine both the age and the erosion rate of a geomorphic surface by analyzing two (or more) different nuclides (Lal, 1991; Gillespie and Bierman, 1995). The results of this approach are commonly illustrated in two-nuclide diagrams, with the concentration of one nuclide on the x-axis and the ratio of the two nuclides on the y-axis (Lal, 1991; see Figure 6). With increasing exposure time, a sample from a surface that does not suffer erosion evolves along a curved trajectory, denoted the *zero-erosion line*. For surfaces eroding at a certain rate the trajectories along which samples evolve are slightly different: their curvatures depend on the erosion rate. In the latter case, the concentrations of both nuclides eventually reach a steady-state and the end points of the curves – for a spectrum of erosion rates – define the *erosion-equilibrium line* (Figure 6). The area between the *erosion-equilibrium line* and the *zero-erosion line* defines the "steady-state erosion island"

(Lal, 1991) and comprises all possible combinations of exposure ages and erosion rates. In other words, a surface that has been continuously exposed to cosmic ray irradiation since formation and has been steadily eroded can only yield data lying within the steady-state erosion island, the exact position depending on the age and the erosion rate. Data points above the erosion-equilibrium line indicate more complex histories that must involve periods of burial during which the production of nuclides slows down or stops. Importantly, the shortest total sample history consistent with any permissible position on the two-nuclide diagram is continuous surface exposure with no erosion, followed by burial sufficiently deep to completely shield the sampled surface from cosmic rays (Bierman et al., 1999). If a sample was exposed at the surface for some time and has subsequently been buried, the minimum time since the initial exposure can therefore be estimated by solving a pair of equations (Bierman et al., 1999). For radioactive nuclides these equations have the form:

$$C = \frac{P}{\lambda}\left[1 - \exp(-\lambda t_e)\right]\exp(-\lambda t_b) \qquad (1)$$

where C is the measured concentration of a cosmogenic nuclide, P the production rate, λ the decay constant, t_e the exposure time, and t_b the burial time. The equivalent equation for stable nuclides is:

$$C = Pt_e \qquad (2)$$

For pairs of different cosmogenic nuclides, e.g. ^{21}Ne and ^{10}Be or ^{10}Be and ^{26}Al, these equations can be solved either analytically or iteratively, and the minimum total time since initial exposure of a sample can be obtained by summing the exposure time t_e and the burial time t_b (Bierman et al., 1999). If the surface has been re-exposed after burial and prior to sampling, which is obviously the case for samples taken at the present-day surface, such calculations will of course underestimate the total exposure history; but in no case can the total history of the sample be less than the calculated total exposure time $t_e + t_b$ (Bierman et al., 1999).

4.2 Sampling, sample preparation, and analytical procedures

All samples are bedrock samples and were taken from quartzite beds, which are widespread in the metamorphosed Paleozoic rocks (Figure 5A; GPS coordinates and altitudes of the sample locations are given in Table 3). Quartzite is resistant to erosion and has been shown to yield reliable ^{21}Ne ages (e.g. Hetzel et al., 2002). The sample sites are located near the flat outer edge of the wave-cut platform, on top of the steep sea cliff, where unweathered bedrock is presently exposed. Farther to the south and away from the cliff, the marine terrace is largely covered by soils and weathering mantles up to a couple of meters thick (Figures 2C, 5B). Sample 03S4 was taken at Punta Los Aguiones, from an exposed bedrock surface near the cliff edge at an elevation of 70 m. The bedrock at Punta Los Aguiones is a quartzite bed at the top of the Cambro-Ordovician Cabos Series. Sample 03S6 was taken at Cape Vidio at an elevation of 90 m. Soil thickness adjacent to the cliff where the sample was taken is less than 0.5 m at present. The sampled quartzite bed also belongs to the Cabos Series. Samples 03S7 and JJ-2-99 are from Cape Vidrias and were taken from quartzitic bedrock exposed at the edge of the 100 m high cliff. Both samples are from quartzite blocks in the Lower Ordovician Barrios Formation. The soil cover in the vicinity of the sample locations is about 0.5 m. Samples 03S8 and JJ-1-99, again from the Barrios Formation, were taken on the western side of Cape Peñas at distances of ~10 m and ~30 m from the cliff edge, respectively. No soil is present in the vicinity of these two sample sites.

After crushing and sieving the samples, the 250-500 μm fraction was chosen for further treatment. Conventional magnetic separation techniques were used to improve the quality of some of these size fractions. The subsequent chemical treatment involved a first leach in HCl at a temperature of ~80°C for 4 hours, followed by a series of three leaches, each between 7 and 10 hours, in a dilute HF/HNO_3 mixture at 80°C in an ultrasonic bath. The etching in the

HF/HNO_3 mixture removed at least several microns of the surfaces of the quartz grains and eliminated meteoric ^{10}Be. The details of the cleaning procedure have been described in Hetzel et al. (2002).

Chemical separation of Be and Al from the purified quartz samples as well as the AMS analysis was performed at Purdue University in the PRIME (Purdue Rare Isotope Measurement) laboratory. Noble gas analysis of the quartz separates was carried out in the noble gas laboratory of the GFZ Potsdam. Gas extraction was accomplished by both stepwise heating and mechanical crushing of aliquots. For crushing, the purified quartz was used without further treatment. The other samples were ground in an agate mill, which resulted in a grain size of <50 μm. Samples were then washed in acetone, dried by heating at ~90°C overnight and wrapped in Al or Ag foil before being loaded into the sample carrousel above the extraction furnace. Samples were degassed in four temperature steps at 400, 600, 800, and 1200 or 1700°C, and the noble gases were analyzed in a VG5400 mass spectrometer.

He, Ne, and Ar isotopes were determined in all temperature steps and by mechanical crushing. The abundances of ^4He and ^{20}Ne and the Ne isotopic compositions are compiled in Table 1. All data have been corrected for analytical blanks, isobaric interferences, and mass discrimination effects. Error limits correspond to the 95% confidence level; they include statistical uncertainties of the measurement, uncertainties of sensitivity and mass discrimination determination, and blank and interference corrections. Further details about analytical procedures and methods of data reduction can be found in Niedermann et al. (1997).

To determine the concentration of cosmogenic ^{21}Ne, we have first plotted the data in a Ne three-isotope diagram. Figure 7 shows these plots for the samples 03S4 and 03S6. Within error limits, the 03S6 data overlap with the spallation line for all heating steps, and the Ne composition determined in the crushed sample is indistinguishable from atmospheric. This

indicates that in 03S6 Ne is a two component mixture of atmospheric and cosmogenic Ne, except for the 1200°C step in which no cosmogenic Ne is released any more (Niedermann, 2002). The total cosmogenic ^{21}Ne concentration is therefore given by the sum of the ^{21}Ne excesses relative to atmospheric composition in the 400-800°C steps. The 03S4 data, however, show a more complex picture. Both the 400°C and 600°C data points lie distinctly below the spallation line, implying the presence of a nucleogenic ^{21}Ne component produced by the $^{18}O(\alpha,n)^{21}Ne$ reaction. In addition, the 1200°C step shows an extremely high $^{21}Ne/^{20}Ne$ ratio of 0.108 (before blank correction), corresponding to ~40% of the total ^{21}Ne excess of this sample, and the ^{4}He concentration is two orders of magnitude higher in 03S4 than in 03S6. These are two more lines of evidence for a major contribution of nucleogenic Ne in 03S4. In such a case, only a relatively rough estimate of the cosmogenic ^{21}Ne concentration is possible, based on the assumption that Ne in the 400-800°C steps is a three-component mixture of atmospheric Ne, cosmogenic Ne, and nucleogenic ^{21}Ne, but without nucleogenic ^{22}Ne.

Table 2 shows how the cosmogenic ^{21}Ne concentrations have been obtained. In the first column, the total ^{21}Ne excess with regard to atmospheric composition is given, while the numbers in the second column have been obtained by correcting for nucleogenic ^{21}Ne according to equation (35) in Niedermann (2002). However, the latter method may yield values higher than the total excess (in particular concerning uncertainties), which is physically meaningless. Therefore, the values assumed for cosmogenic ^{21}Ne and given in the third column are always smaller than or equal to those in the first column, which also leads to asymmetric error limits in many cases. The cosmogenic ^{21}Ne concentrations given in the third column of Table 2 have been used for the calculations presented in the following section.

4.3 Results

Evaluation of the measured concentrations of cosmogenic nuclides requires the use of an exposure model and the scaling of the production rates to the sampling sites. We applied the scaling method of Dunai (2000) and used the ^{21}Ne production rate of 19.0±3.7 at g^{-1} a^{-1} of Niedermann (2000) and the production rates for ^{10}Be and ^{26}Al from Kubik et al. (1998). Since Kubik et al. (1998) applied the scaling method of Lal (1991) to convert their measured concentrations to sea level and high latitude, we have first converted their original data with the method of Dunai (2000) to sea level and high latitude and obtained production rates for ^{10}Be and ^{26}Al of 5.42±0.46 and 35.2±3.6 at g^{-1} a^{-1}, respectively (all errors are reported at the 2σ level). These rates were then scaled to the study sites. The resulting production rate ratios are 3.51±0.74 for ^{21}Ne/^{10}Be and 0.54±0.12 for ^{21}Ne/^{26}Al. We did not make any corrections for a temporal variation of the production rates, as time-integrated production rates at latitude 40°N should deviate by ~6% at most from the present-day values (Dunai, 2001), and possibly much less than that (<2%; Masarik et al., 2001).

In a first step we calculate minimum exposure ages using the three cosmogenic nuclides ^{21}Ne, ^{10}Be and ^{26}Al separately. In order for the ages to be geologically meaningful this approach requires a continuous exposure of the analyzed samples at the very surface. Both, removal of material from the original bedrock surface or temporal burial of the wave-cut platform – for instance beneath water during sea level highstands or owing to deposition of marine sediments on the bedrock – would increase the age. As a consequence, the calculated ages obtained for the three nuclides (Table 3) are *minimum* ages for the marine terrace (e.g. Niedermann, 2002).

In order to evaluate whether the samples were ever shielded due to temporary burial, the results are plotted in two-nuclide diagrams (Figure 6). As outlined above, a geomorphic surface that has been continuously exposed to cosmic ray irradiation since formation and has been steadily eroded can only yield data lying between the zero erosion and the erosion

equilibrium lines, the exact position depending on the age and the erosion rate (Fig. 6). The fact that three out of four samples plot above the erosion equilibrium line in the ^{21}Ne-^{10}Be diagram demonstrates that they were partly or completely shielded after initial exposure (e.g. Lal, 1991). At least for sample 03S6, this conclusion is also supported by the ^{10}Be-^{26}Al plot. Such shielding or burial allows the radioactive nuclides ^{10}Be and ^{26}Al to decay according to their half-lives of 1.5 and 0.7 Ma, respectively (Lal, 1991). It is this process that also causes the minimum exposure ages calculated for the different nuclides to differ from one another (Table 3).

By using equations (1) and (2) given above, the minimum times since initial exposure have been quantified for both pairs ^{10}Be-^{26}Al and ^{21}Ne-^{10}Be for the four samples 03S4, 03S6, 03S7, and 03S8 (Table 4). The minimum times that are based on ^{10}Be-^{26}Al generally turn out smaller than those based on ^{21}Ne-^{10}Be, which is not unexpected since very old periods of exposure tend to be "forgotten" by relatively short-lived ^{26}Al. Therefore, the ^{21}Ne-^{10}Be data impose a more stringent lower limit on the total exposure and burial time, except for sample 03S6 which yields similar numbers for both pairs. The most probable values for the *minimum total ages* – based on the combined nuclides ^{21}Ne and ^{10}Be – are 2290 ka, 2120 ka and 1440 ka for three out of four investigated samples. The fourth sample (03S8) yields a *minimum total age* of 300 (+2500/-110) ka. Considering the large positive error limit of the latter age, the result of sample 03S8 is entirely consistent with those of the three other samples. The error limits of the ^{21}Ne-^{10}Be-based times have been analytically derived using common error propagation, while those for the ^{10}Be-^{26}Al-based times are only crude estimates as we did not perform Monte Carlo calculations to derive them (cf. Bierman et al., 1999). For the ^{21}Ne-^{10}Be-based data of sample 03S8, however, the lower error limits of the minimum exposure and minimum total times were not obtained by error propagation, but by considering the fact that the minimum age cannot be lower than the lower error limit of the ^{10}Be single-

nuclide age (Tables 3, 4). The same criterion was used for the ^{10}Be-^{26}Al-based data of 03S4.

5. Discussion

Our cosmogenic nuclide data set – derived from bedrock samples of an extensive marine terrace in northern Spain – highlights the advantage of using several different cosmogenic nuclides (^{21}Ne, ^{10}Be and ^{26}Al) in order to derive age constraints for surfaces that have experienced significant periods of burial and thus shielding from cosmic rays. Minimum exposure ages calculated separately for each of these three nuclides range from ~100 ka to ~500 ka (Table 3). In contrast, the nominal *minimum* ages based on the combination of the nuclides ^{21}Ne and ^{10}Be are considerably higher, i.e. 2290 ka, 2120 ka and 1440 ka for three samples (Table 4). The lower error limits of the ^{21}Ne-^{10}Be-based minimum total times represent absolute lower limits at the 95% confidence level to the time since initial exposure began. These lower limits correspond to 1390, 1050, and 880 ka for the samples 03S4, 03S6, and 03S7, respectively. 03S6 yields a similar lower limit of ~1180 ka for the pair ^{10}Be-^{26}Al. Assuming that the whole terrace was formed during a time interval short compared to its subsequent history (see below), the highest of these values should give the absolute minimum age of the terrace, which would be 1.4 Ma (sample 03S4, see above). However, as 03S4 contained a lot of nucleogenic Ne, its result may be less reliable. 03S6 and 03S7 both yield minimum ages of ~1 Ma (~1.1 and 0.88 Ma, respectively), which we interpret as a safe lower limit for the initial formation of the terrace. Thus, we interpret the wave-cut platform to be at least 1 Ma, but probably more than 1.5 to 2 Ma old. We emphasize that only a lower but no upper age limit can be inferred from the cosmogenic nuclide data.

The great width of the marine terrace of 2–4 km and the fact that it was carved into very resistant bedrock suggests that it was generated during an extended period of time; at least several tens of thousand and probably up to a few hundred thousand years. The

successive re-occupation of the widening platform during several consecutive sea level highstands seems to be the only feasible mechanism to generate such a wide platform (cf. Kelsey and Bockheim, 1994; Burbank and Anderson, 2001). As the vertical extent of the marine terrace is about 40 to 70 m (see Figure 4), the difference in sea level between the consecutive highstands must have reached a similar value (the difference between sea level low and high stands was presumably even larger). According to the eustatic sea level curve of Miller et al. (2005, their figure 4), sea level fluctuations in the Late Miocene and Early Pliocene, i.e. before ~3.0 Ma, did not exceed 30-60 m. Only after ~3 Ma did the amplitude of the sea level variations gradually increase (Ruddiman and Raymo, 1988; Shackleton et al., 1990; Miller et al. 2005) and eventually reached 120-130 m, the value well documented for the last climate cycle (e.g. Shackleton, 1987). These considerations on the magnitude of past sea level variations – combined with our *minimum* age estimate for the marine terrace of 1-2 Ma – suggest that the wave-cut platform formed in the course of the Pliocene, when the increase in the amplitude of the sea level variations caused a progressive widening of the wave-cut platform during consecutive sea level highstands (Figure 8A). Our analysis is in agreement with the previous age estimate by Mary (1983) which was only based on relative age constraints such as the thickness of weathering mantles and stratigraphic relations.

What remains unknown is the onset of platform formation as well as the time when the marine terrace emerged from the sea due to rock uplift (Figure 8B). The progressive eastward increase in the elevation of the marine terrace and the paleoshoreline angle clearly demonstrates that the amount of rock uplift has spatially varied along the coast (Figures 4, 5). A spatial decrease in the uplift rate to the west could explain why the platform width increases in that direction (Figure 3). By combining the mean of our minimum age of 1-2 Ma for the terrace, i.e. 1.5 Ma, with the present-day elevation of the paleoshoreline angle of 100-220 m, we infer a maximum rock uplift rate of 0.07 to 0.15 mm/a. This calculation implicitly

assumes that the elevation of the sea level during highstands did not change significantly since the onset of platform uplift in the Pliocene or Early Quaternary, which is confirmed by the sea level curve of Miller et al. (2005). In other words, the total amount of rock uplift should be equal to the elevation of the paleoshoreline angle above the present-day sea level (Figure 8B). The vertical displacements of 20-40 m observed on the faults cutting the paleoshoreline angle (Figure 5A) have accumulated after the uplift of the terrace (Figure 8C). Combining again the mean of the minimum age estimate for the terrace, i.e. 1.5 Ma, with the observed vertical offsets of the paleoshoreline angle yields maximum vertical slip rates on the order of 0.01-0.03 mm/a. Whether faulting had already started prior to the emergence of the terrace is not known, however, in that case any submarine fault scarps would probably have been destroyed due to erosion by waves.

The low maximum uplift rate of ~0.1 mm/a proposed for the Asturian coast may result from ongoing Quaternary shortening along the northern edge of the Iberian plate. From the Eocene onwards the subduction of oceanic crust in the Bay of Biscay beneath the Iberian continental margin led to the formation of an incipient subduction zone (Figure 9) (Sibuet and Le Pichon, 1971; Boillot et al., 1979; Grimaud et al., 1982; Roest and Srivastava, 1991; Alvarez-Marrón et al., 1997). The subduction continued until the Early Miocene (Boillot et al., 1979; Roest and Srivastava, 1991), and possibly into the Neogene (Alvarez-Marrón et al., 1996, 1997). Onshore the youngest documented shortening structures formed in the Neogene (Espina et al., 1996), late Tertiary (Alonso et al., 1996), and Aquitanian (Huerta et al., 1996). Late Miocene and Pliocene E-W trending faults have locally been described in the Cantabrian Mountains (Andeweg, 2002). The Quaternary faulting that affects the morphology of the marine terrace documented in this study is the youngest deformation so far described at the north coast of Spain. It is compatible with NNW-SSE to NW-SE directed compression in the northwestern part of Iberia inferred from seismic activity, earthquake focal mechanisms and

paleostress studies (Herraiz et al., 2000; López et al., 2004), and also with the slower motion of convergence between Iberia and Europe since the Early Miocene (Rosenbaum et al., 2002).

6. Conclusions

This study provides the first quantitative age constraints for a very broad marine terrace, extending for ~100 km along the coast of northern Spain. Measurements of multiple cosmogenic nuclides (^{21}Ne, ^{10}Be, ^{26}Al) indicate that the terrace is at least 1-2 Ma old and is thus among the oldest landforms of this type. The morphology of the terrace, its age, and the elevation of the paleoshoreline angle, allow us to infer a very low rock uplift rate. Owing to the gradual eastward increase of terrace elevation the inferred maximum rock uplift rate rises eastward from ~0.07 to ~0.15 mm/a. Abrupt local changes in the elevation of the paleoshoreline angle are associated with faults that have accumulated vertical throws of several tens of meters since the emergence of the platform. Faulting of the marine terrace implies that the northern Iberian plate underwent crustal deformation in younger times than previously documented. This study has shown that the use of digital terrain models is a powerful tool when analysing coastal landforms such and marine terraces and to automatically map the associated paleoshoreline angle.

Acknowledgements

This research was funded by the Spanish Ministry of Education and Science, through projects BTE2002-00330 from the National Research Plan and project CGL2005-24204, and by the GeoForschungsZentrum Potsdam. We thank Robert Weisz for his help in calculating the mimimum ages using the combined ^{10}Be and ^{26}Al concentrations and Enzio Schnabel for performing the noble gas analyses. The valuable suggestions of three anonymous reviewers helped to improve the manuscript.

Figure captions

Fig. 1: Idealized sketch of a rocky coast illustrating the terminology used in this study (modified from Burbank and Anderson, 2001). A broad wave-cut platform is preserved above sea level due to uplift of a landmass. The uplifted marine terrace comprises the wave-cut platform and, locally, a thin cover of marine sediments (not shown). The shoreline angle refers to the intersection between the presently eroding wave-cut platform and the sea cliff. It marks the average sea level over many tidal cycles. The paleoshoreline angle marks the former shoreline of the uplifted marine terrace and provides a paleohorizontal marker.

Fig. 2: A) Color-shaded map showing the land and sea floor topographies of the Bay of Biscay and surrounding French and Spanish continental masses. Note the contrasting morphology of the French and Spanish margins surrounding the Bay of Biscay. On the Spanish side a coastal mountain chain (Cantabrian Mountains) stretches along the coast next to a narrow continental margin platform, while on the French side the continental margin platform is wide and the onshore relief is low. B) Digital elevation model (DEM) of the Cantabrian Mountains that reach a maximum elevation of more than 2500 m in the Picos de Europa Massif about 50 km from the coast. White box shows location of the studied coastal sector that appears in Figure 3. C) Photograph of the marine terrace at Cape Vidio showing west-dipping and well bedded Ordovician quartzites.

Fig. 3: A) Digital elevation model of the western Asturias coastal region with a horizontal resolution of 10 m. The DEM was constructed from digital elevation data at 1: 5,000 scale with a contour interval of 5 m. Base topographic maps are from the Cartographic Service of the regional government of the *Principado de Asturias*. Four major estuaries incised into the marine terrace are indicated. B) SLOPE model constructed from the DEM. Areas with slopes

less than 5º are shown in orange and superposed by contour lines with 20 m interval. Elevation values for some contours are indicated. The slopes were calculated by fitting a plane to the elevation values of a 3x3 cell neighbourhood around the processing cell, in which the slope is calculated using the average maximum technique (Burrough, 1986).

Fig. 4: Four topographic profiles across the marine terrace constructed from 1:25,000 scale topographic maps. The paleoshoreline angle marks the inland edge of the marine terrace (see Figure 5). Note the variable vertical extent of the marine terrace, calculated as the elevation difference between the paleoshoreline angle and the sea cliff: 70 m on profiles 1 and 2, and 60 and 40 m in profiles 3 and 4, respectively.

Fig. 5: A) Geological map of the terrace including marine and continental cover deposits as well as soils and weathering mantles (taken from the Environmental Thematic Map, INDUROT, 1989-2001). The Paleozoic Narcea thrust separates metamorphosed from non-metamorphic sediments (see Alonso et al., 1991 for detailed geological map of the basement). The location of the paleoshoreline angle is shown as a thick blue line with the altitude in meters indicated as blue numbers. Faults that displace the paleoshoreline angle are shown in red (see text for further explanation). The blue numbers along the coastline indicate the local elevation of the sea cliff. The dip direction of the marine terrace in each fault-bounded block is shown by black arrows. B) Field photograph of a strike-slip fault located ~3 km SSE of Cape Busto at an elevation of 90 m (road cut near kilometer 150 of the road N-632). The main fault is subvertical and offsets the contact between basement rocks and overlying marine deposits by ~2 m.

Fig. 6. Two-nuclide plots of $^{10}Be/^{26}Al$ versus ^{26}Al (A) and $^{21}Ne/^{10}Be$ versus ^{10}Be (B) showing

the positions of the four samples for which the concentrations of all three nuclides have been determined (label x denotes sample 03Sx). Data for samples experiencing simple exposure histories should plot within the area confined by the "zero erosion" and the "erosion equilibrium" lines (e.g. Lal, 1991). The dotted lines show evolution paths of surfaces irradiated at constant erosion rates of 10, 1, 0.1, and 0.01 m/Ma; in these cases cosmogenic nuclide concentrations remain constant when the erosion equilibrium line is reached. The positions of the four samples from the marine terrace indicate that at least three of them must have experienced a complex exposure history including one or more significant periods of burial. Error limits are 2σ; for further explanation see text.

Fig. 7. Ne three-isotope plots for samples 03S6 (A) and 03S4 (B). Open squares show data from stepwise heating extractions (labelled with temperature in °C), closed squares represent crushing data. Error limits are 2σ. The 1200º C data have not been corrected for blanks, because due to low gas amounts, the blank correction introduces large uncertainties, moving the data farther away from atmospheric but leaving the general picture unchanged. Data for 03S6 are aligned along the spallation line (Niedermann et al., 1993), indicating a two-component mixture of atmospheric and cosmogenic Ne for the heating steps 400-800°C, while the 1200°C step shows the presence of a minor amount of nucleogenic Ne (~8% of total excess ^{21}Ne). In contrast, most 03S4 data lie below the spallation line, reflecting a substantial contribution of nucleogenic ^{21}Ne. This inference is supported by the 1200°C data (inset in Fig. 7B), corresponding to a 40% fraction of the total ^{21}Ne excess, and by a two order-of-magnitude higher ^{4}He content in 03S4 than 03S6 (Table 1). The composition of Ne trapped in fluid inclusions as obtained by crushing the quartz is very close to atmospheric for both samples.

Fig. 8. Proposed scenarios for the evolution of the marine terrace in western Asturias. A) Widening of a wave-cut platform occurs by inland migration of the shoreline during consecutive sea level highstands. B) Rock uplift leads to emergence of the terrace. Sea level at the onset of uplift is assumed to be the same as today. C) Present-day configuration of the marine terrace. After emergence of the marine terrace the tectonic displacements on faults cutting the paleoshoreline angle and the terrace are preserved.

Fig. 9: A) Simplified geological map of northwestern Spain (modified from Boillot and Malod, 1988). Offshore, the Eocene-Miocene accretionary prism and NW-SE trending strike-slip faults in the continental margin are indicated. The onshore geology includes the major Alpine faults (thicker lines) and the Ebro-Duero foreland basins of the Pyrenean-Cantabrian chain. The main Paleozoic structures within the Variscan Basement are represented as thin black lines, in particular the Narcea Thrust that separates the external Variscan zone (Cantabrian Zone) from metamorphosed Variscan rocks in the hinterland. The vertical black line marks the location of the section shown in B. The dashed box corresponds to the area of figure 2B. A thick grey line marks the portion of shoreline analyzed. B) Schematic crustal-scale cross-section showing the structure of the northern edge of the Iberian plate (modified from Alvarez-Marrón et al., 1997). The section is based on seismic data ESCIN-4 offshore and ESCIN-2 onshore (Alvarez-Marrón et al., 1996; Pulgar et al., 1996; Fernandez-Viejo, 1997).

References

Alonso, J.L., Aller, J., Bastida, F., Marcos, A., Marquínez, J., Perez Estaun, A., Pulgar, J.A., 1991. Mapa Geológico de España (Escala 1 :200.000). Hoja de Avilés. Instituto Geológico y Minero de España, Madrid.

Alonso, J. L., Pulgar, J.A., García-Ramos, J.C., Barba, P., 1996. Tertiary basins and Alpine tectonics in the Cantabrian Mountains (NW Spain). In: Friend, P.F., Dabriao, C., Tertiary Basins of Spain: Tectonics, Climate and Sea-level Changes. Cambridge Univ. Press, Cambridge, pp. 214-227.

Alvarez-Marrón, J., Pérez-Estaún, A., Dañobeitia, J.J., Pulgar, J.A., Martínez Catalán, R., Marcos, A., Bastida, F., Ayarza Arribas, P., Aller, J., Gallart, A., Gonzalez-Lodeiro, F., Banda, E., Comas, M.C., Cordoba, D., 1996. Seismic structure of the northern continental margin of Spain from ESCIN deep seismic profiles. Tectonophysics 264, 153-174.

Alvarez-Marrón, J., Rubio, E., Torne, M., 1997. Subduction-related structures in the North Iberian Margin. J. Geophys. Res. 102, 22497-22511.

Anderson, R.S., Densmore, A.L., Ellis, M.A., 1999. The generation and degradation of marine terraces. Basin Research 11, 7-19.

Andeweg, B., 2002. Cenozoic tectonic evolution of the Iberian Peninsula causes and effects of changing stress fields. Ph.D. Thesis, Vrije Universiteit Amsterdam, ISBN 90-9015593-7. Netherlands Research School of Sedimentary Geology, publication no. 20020101.

Bierman, P.R., Marsella, K.A., Patterson, C., Thompson Davis, P., Caffee, M., 1999. Mid-Pleistocene cosmogenic minimum-age limits for pre-Wisconsinan glacial surfaces in southwestern Minnesota and southern Baffin Island: a multiple nuclide approach. Geomorphology 27, 25-39.

Boillot, G., Dupeuble, P.A., Malod, J., 1979. Subduction and tectonics on the continental margin off northern Spain. Marine Geology 32, 53-70.

Boillot, G., Malod, J., 1988. The north and north-west Spanish continental margin: a review. Revista de la Sociedad Geológica de España 1, 295-316.

Bradley, W.C., Griggs, G.B., 1976. Form, genesis, and deformation of central California wave-cut platforms. Geological Society of America Bulletin 87, 433-449.

Burbank, D.W., Anderson, R.S., 2001. Tectonic geomorphology. Blackwell Science, USA.

Burrough, P.A., 1986. Principles of Geographical Information Systems for Land Resources Assessment. Oxford University Press, New York.

Chappell, J., Omura, A., Esat, T., McCulloch, M., Pandolfi, J., Ota, Y., Pillans, B., 1996. Reconciliation of late Quaternary sea levels derived from coral terraces at Huon

Peninsula with deep sea oxygen isotope records. Earth and Planetary Science Letters 141, 227-236.

Dunai, T.J., 2000. Scaling factors for production rates of in situ produced cosmogenic nuclides: a critical reevaluation. Earth and Planetary Science Letters 176, 157-169.

Dunai, T.J., 2001. Influence of secular variation of the geomagnetic field on production rates of in situ produced cosmogenic nuclides. Earth and Planetary Science Letters 193, 197-212.

Espina, R.G., Alonso, J.L., Pulgar, J.A., 1996. Growth and propagation of buckle folds determined from syntectonic sediments (the Ubierna Fold Belt, Cantabrian Mountains, N Spain). J. Struct. Geol. 18(4) 431-441.

Fernandez, F.J., Menéndez Duarte, R., Marquínez, J., 1997. Aplicación de un sistema de información geográfica a la cartografía temática y clasificación geomorfológica de los sistemas fluviales en Asturias. Revista de la Sociedad Geológica de España 10(1-2), 117-129.

Fernandez-Viejo, G., 1997. Estructura cortical de la Cordillera Cantábrica y su transición a la Cuenca del Duero, a partir de datos de sísmica de refracción/reflexión de gran ángulo. Ph.D. Thesis. Univ. Barcelona, Spain.

Flor, G., 1983. Las rasas asturianas: ensayos de correlación y emplazamiento. Trabajos de Geologia, Universidad de Oviedo, 13, 65-81.

Gillespie, A.R., Bierman, P.R., 1995. Precision of terrestrial exposure ages and erosion rates estimated from analysis of cosmogenic isotopes produced in situ. J. Geophys. Res. 100 (B12), 24, 637-649.

Gosse, J.C., Phillips, F.M., 2001. Terrestrial in situ cosmogenic nuclides: theory and application. Quaternary Science Reviews 20, 1475-1560.

Grant, L.B., Mueller, K.J., Gath, E.M., Cheng, H., Edwards, R.L., Munro, R., Kennedy, G.L., 1999. Late Quaternary uplift and earthquake potential of the San Joaquin Hills, southern Los Angeles basin, California. Geology 27, 1031-1034.

Grimaud, S., Boillot, G., Collete, B.J., Mauffret, A., Miles, P.R., Roberts, D.B., 1982. Western extension of the Iberian-European plate boundary during Early Cenozoic (Pyrenean) convergence: A new model. Marine Geology 45, 63-77.

Herraiz, M., De Vicente, G., Lindo-Ñaupari, R., Giner, J., Simón, J.L., Gonzalez-Casado, J.M., Vadillo, O., Rodríguez-Pascua, M.A., Circuéndez, J.I., Casa, A., Cabañas, L., Rincón, P., Cortés, A.L., Ramírez, M., Lucini, M., 2000. The recent (Upper Miocene to

Quaternary) and present tectonic stress distribution in the Iberian peninsula. Tectonics 19, 762-786.

Hetzel, R., Niedermann, S., Ivy-Ochs, S., Kubik, P.W., Tao, M., Gao, B., 2002. ^{21}Ne versus ^{10}Be and ^{26}Al exposure ages of fluvial terraces: the influence of crustal Ne in quartz. Earth and Planetary Science Letters 201, 575-591.

Hsieh, M.L., Liew, P.M., Hsu, M.Y., 2004. Holocene tectonic uplift on the Hua-tung coast, eastern Taiwan. Quaternary International 115-116, 47-70.

Huerta, A., Parés, J.M., Cabrera, L., Ferrús, B., Sáez, A, 1996. Datación magnetoestratigráfica de la cuenca terciaria de As Pontes (Galicia, NW España), Geogaceta 20, 1021-1024.

Julivert, M., 1987. The structure and evolution of the Hercynian fold belt in the Iberian Peninsula. In: Schaer, J.P., Rodgers, J., The anatomy of mountain belts. Princeton Univ. Press, Princeton, NJ, pp. 65-102.

Kelsey, H.M., Bockheim, J.G., 1994. Coastal landscape evolution as a function of eustasy and surface uplift rate, Cascadia margin, southern Oregon. Geological Society of America Bulletin 106, 840-854.

Kim, K.J., Sutherland, R., 2004. Uplift rate and landscape development in southern Fiordland, New Zealand, determined using ^{10}Be and ^{26}Al exposure dating of marine terraces. Geochimica et Cosmochimica Acta 68, 2313-2319.

Kubik, P.W., Ivy-Ochs, S., Masarik, J., Frank, M., Schlüchter, C., 1998. ^{10}Be and ^{26}Al production rates deduced from an instantaneous event within the dendro-calibration curve, the landslide of Köfels, Ötz Valley, Austria. Earth and Planetary Science Letters 161, 231-241.

Lal, D., 1991. Cosmic ray labeling of erosion surfaces: in situ nuclide production rates and erosion models. Earth and Planetary Science Letters 104, 424-439.

López, C., Pulgar J.A., Gallart, J., González-Cortina, J.M., Ruíz, M., 2004. Present seismicity and tectonics in the NW Iberian Peninsula (Spain): results from the GASPI Project. Geophysical Research Abstracts, vol. 6, 04142. SRef-ID: 1607-7962/gra/EGU04-A-04142. European Geosciences Union.

Marquardt, C., Laveneu, A., Ortlieb, L., Godoy, E., Comte, D., 2004. Coastal neotectonics in Southern Central Andes: uplift and deformation of marine terraces in Northern Chile (27ºS). Tectonophysics 394, 193-219.

Marquínez, J., 1992. Relieve y tectónica reciente en la Cornisa Cantábrica. In: Cearreta Y., Ugarte, F. (Eds.), The Quaternary in the Western Pyrenean Region, Universidad del País Vasco, pp. 143-159.

Mary, G., 1983. Evolución del margen costero de la Cordillera Cantábrica en Asturias desde el Mioceno. Trabajos de Geología 13, 3-35.

Mary, G., 1985. Niveaux marins du littoral asturien et galicien entre San Vicente de la Barquera et Foz. I Reunión del Cuaternario Ibérico. Lisboa, pp. 219-228.

Masarik, J., Frank, M., Schäfer, J.M., Wieler, R., 2001. Correction of *in situ* production rates for geomagnetic field intensity variations during the past 800,000 years. Geochimica Et Cosmochimica Acta 65, 2995-3003.

Merritts, D., Bull, W.B., 1989. Interpreting Quaternary uplift rates at the Mendocino triple junction, northern California, from uplifted marine terraces. Geology 17, 1020-1024.

Miller, K.G., Kominz, M.A., Browning, J.V., Wright, J.D., Mountain, G.S., Katz, M.A., Sugarman, P.J., Cramer, B.S., Christie-Blick, N., Pekar, S.F., 2005. The Phanerozoic record of global sea-level change. Science 310, 1293-1296.

Moñino, M., Díaz de Terán, J.R., Cendrero, A., 1988. Pleistocene sea level changes in the Cantabrian coast Spain. In: Singh, S., Tiwari, R.C. (Eds.), Geomorphology and Environment. The Allahabad Geogr. Soc., Allahabad, India, pp. 351-364.

Niedermann, S., Graf, Th., Marti, K., 1993. Mass spectrometric identification of cosmic-ray-produced neon in terrestrial rocks with multiple neon components. Earth and Planetary Science Letters 118, 65-73.

Niedermann, S., Bach, W., Erzinger, J., 1997. Noble gas evidence for a lower mantle component in MORBs from the southern East Pacific Rise: Decoupling of helium and neon isotope systematics. Geochimica et Cosmochimica Acta 61, 2697-2715.

Niedermann, S., 2000. The ^{21}Ne production rate in quartz revisited. Earth and Planetary Science Letters 183, 361-364.

Niedermann, S., 2002. Cosmic-ray produced noble gases in terrestrial rocks: Dating tools for surface processes. In: Porcelli, D., Ballentine, C.J., Wieler, R. (Eds.), Noble Gases in Geochemistry and Cosmochemistry, Reviews in Mineralogy and Geochemistry 47, 731-784.

O'Neal, M.L., McGeary, S., 2002. Late Quaternary stratigraphy and sea-level history of the northern Delaware Bay margin, Southern New Jersey, USA: a ground penetrating radar analysis of composite Quaternary coastal terraces. Quaternary Science Reviews 21, 929-946.

Pérez-Estaún, A., Bastida, F., Martínez-Catalán, J.R., Gutiérrez-Marco, J.C., Marcos, A., Pulgar, J.A., 1990. West Asturian-Leonese Zone: Stratigraphy. In: Dallmeyer, R.D.,

Martinez García, E. (Eds.), Pre-Mesozoic Geology of Iberia. Springer-Verlag, pp. 92-102.

Pérez-Estaún, A., Martínez-Catalán, J.R., Bastida, F., 1991. Crustal thickening and deformation sequence in the footwall to the suture of the Variscan belt of northwest Spain. In: Pérez-Estaún, A., Coward, M.P. (Eds.), Deformation and Plate Tectonics. Tectonophysics 191, 243-253.

Perg, L.A., Anderson, R.S., Finkel, R.C., 2001. Use of a new ^{10}Be and ^{26}Al inventory method to date marine terraces, Santa Cruz, California, USA. Geology 29, 879-882.

Pulgar, J., Gallart, J., Fernández-Viejo, G., Pérez-Estaún, A., Alvarez-Marrón, J., ESCIN Group, 1996. Seismic image of the Cantabrian Mountains uplift in the western extension of the Pyrenean Belt from integrated ESCIN reflection and refraction data. Tectonophysics 264, 1-20.

Roest, W.R., Srivastava, S.P., 1991. Kinematics of the plate boundaries between Eurasia, Iberia, and Africa in the North Atlantic from Late Cretaceous to the present. Geology 19, 613-616.

Rosenbaum, G., Lister, G.S., Duboz, C., 2002. Relative motions of Africa, Iberia and Europe during Alpine orogeny. Tectonophysics 359, 117-129.

Ruddiman W.F., Raymo, M.E., 1988. Northern hemisphere climate regimes during the past 3 Ma: possible tectonic connections. Phil. Trans. R. Soc. Lond. B 318, 411-430.

Shackleton, N.J., 1987. Oxygen isotopes, ice volume and sea level. Quaternary Science Reviews 6, 183-190.

Shackleton, N.J., Berger, A., Peltier, W.R., 1990. An alternative astronomical calibration on the Lower Pleistocene time scale based on ODP site 677. Trans. Soc. Edinburgh Earth Sci. 81, 251-261.

Sibuet, J.C., Le Pichon, X., 1971. Structure gravimétrique du Golfe de Gascogne a partir des profils de sismique. In: Debysier, J., Le Pichon, X., Montadert, M. (Eds.), Histoire structurale du Golfe de Gascogne. Technip, Paris, VI.9.11-VI.9.18.

Stone, J., Lambeck, K., Fifield, L.K., Evans, J.M., Cresswell, R.G., 1996. A Lateglacial age for the Main Rock Platform, Western Scotland. Geology 24, 707-710.

Westaway, R., Bridgland, D., White, M., 2006. The Quaternary uplift history of central southern England: evidence from the terraces of the Solent River system and nearby raised beaches. Quaternary Science Reviews 25, 2212-2250.

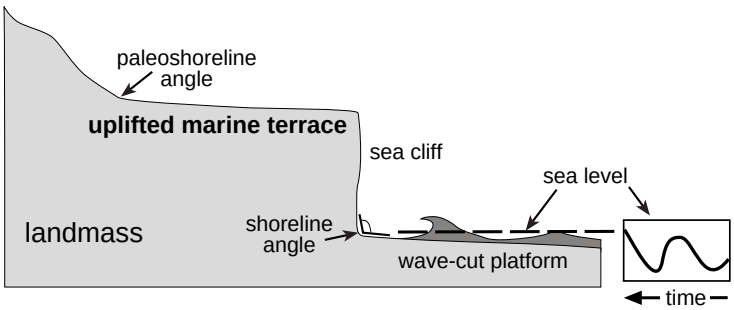

Figure 1. Alvarez-Marron et al.

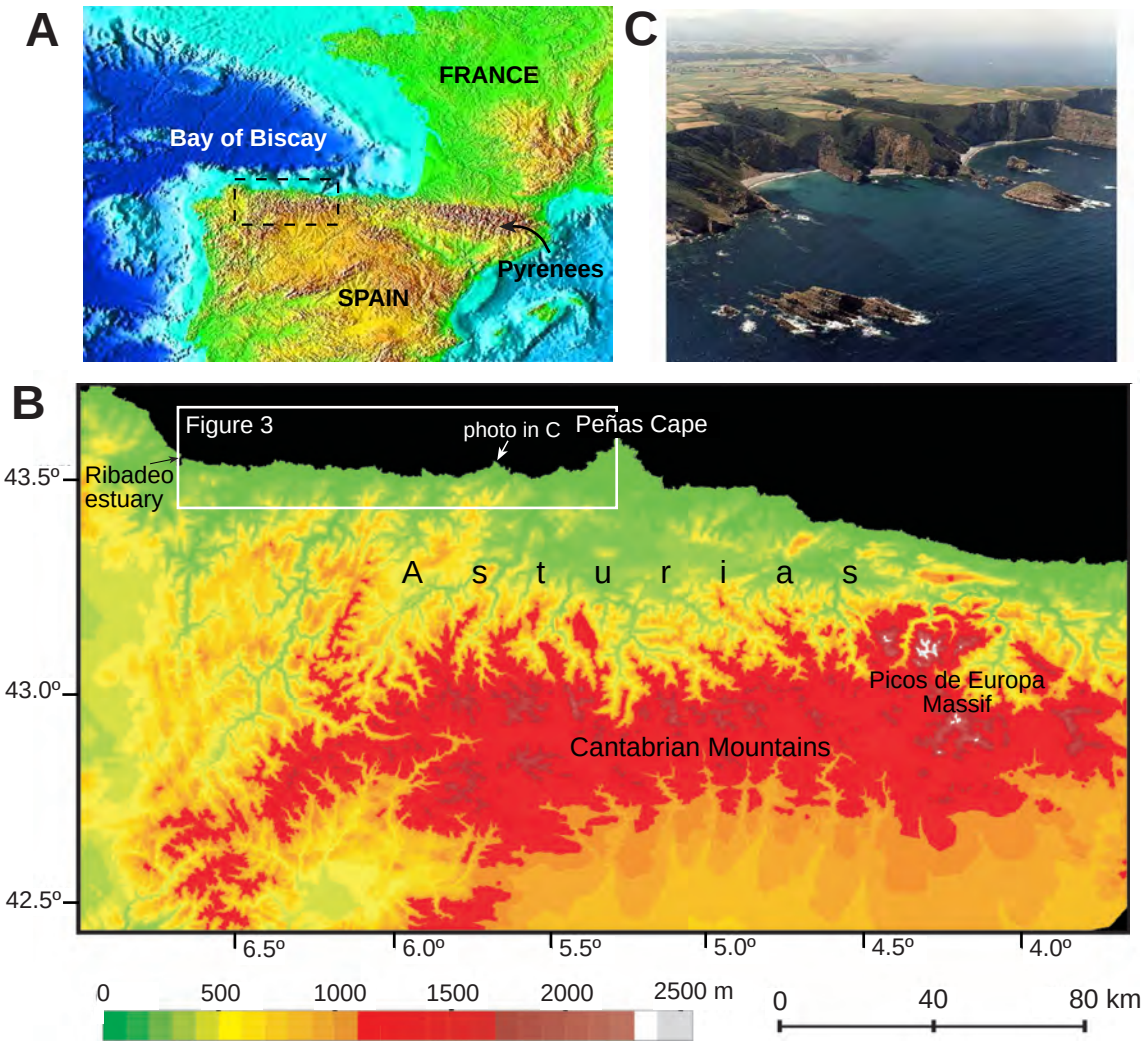

Figure 2. Alvarez-Marron et al.

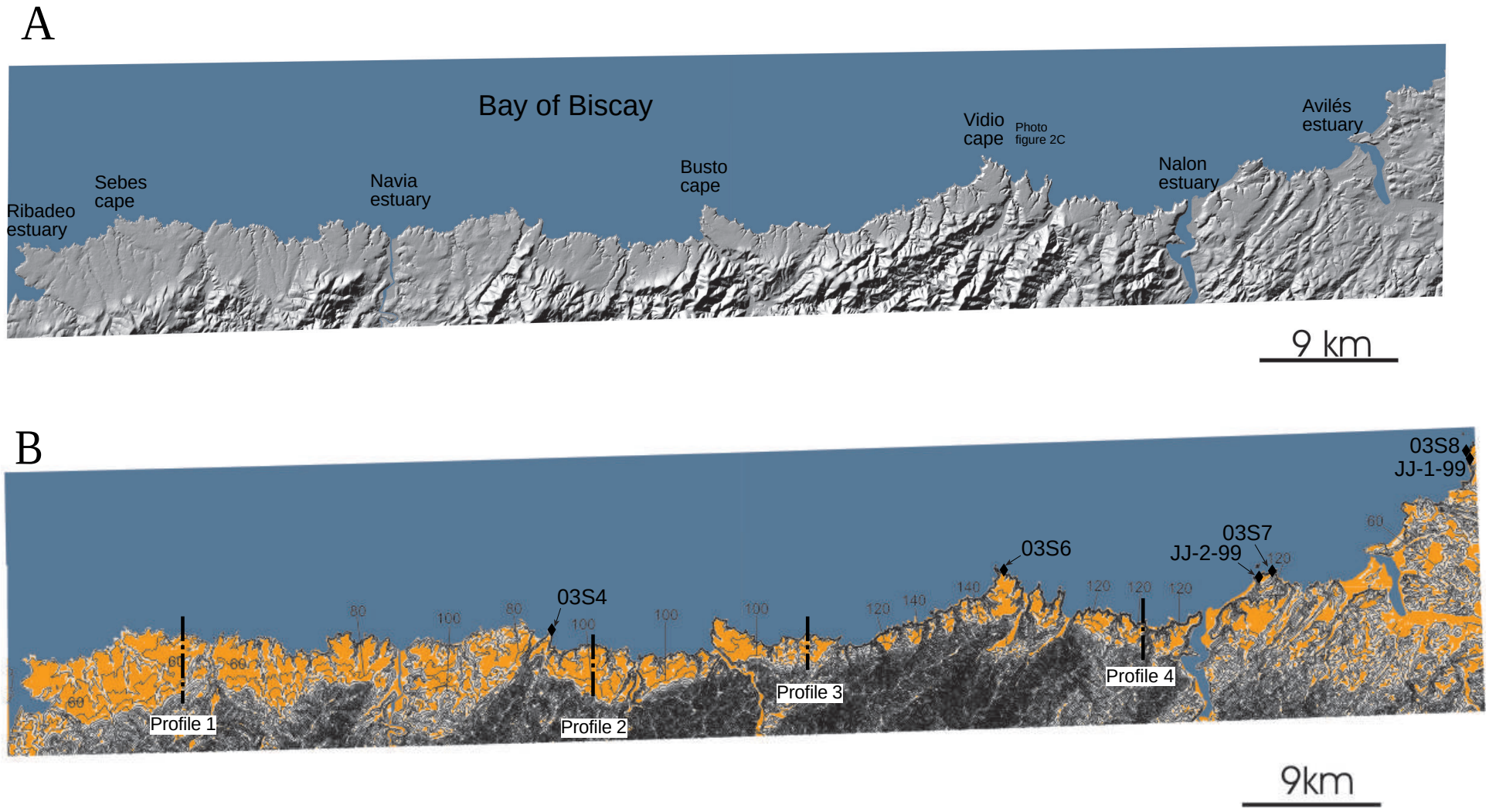

Figure 3. Alvarez-Marron et al.

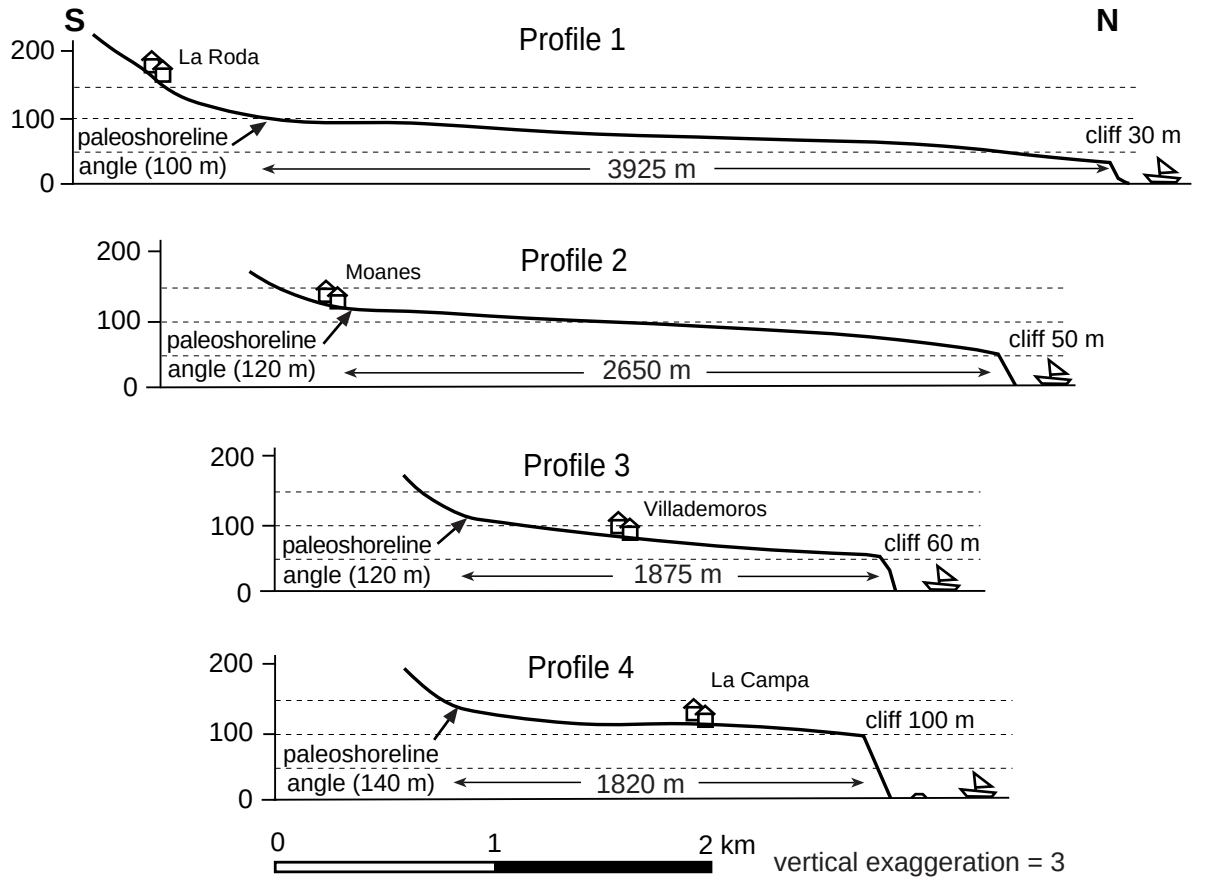

Figure 4. Alvarez-Marron et al.

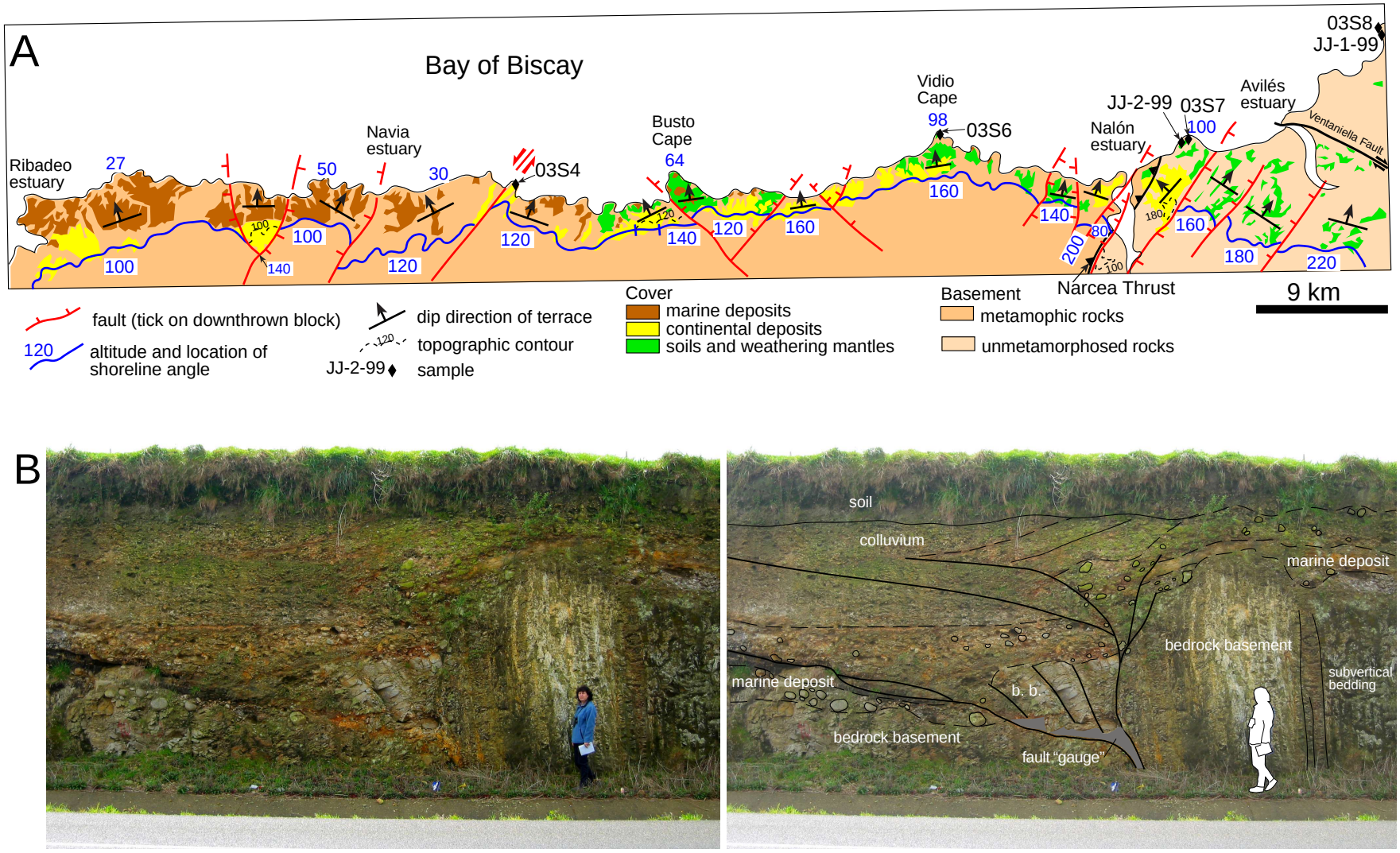

Figure 5. Alvarez-Marron et al.

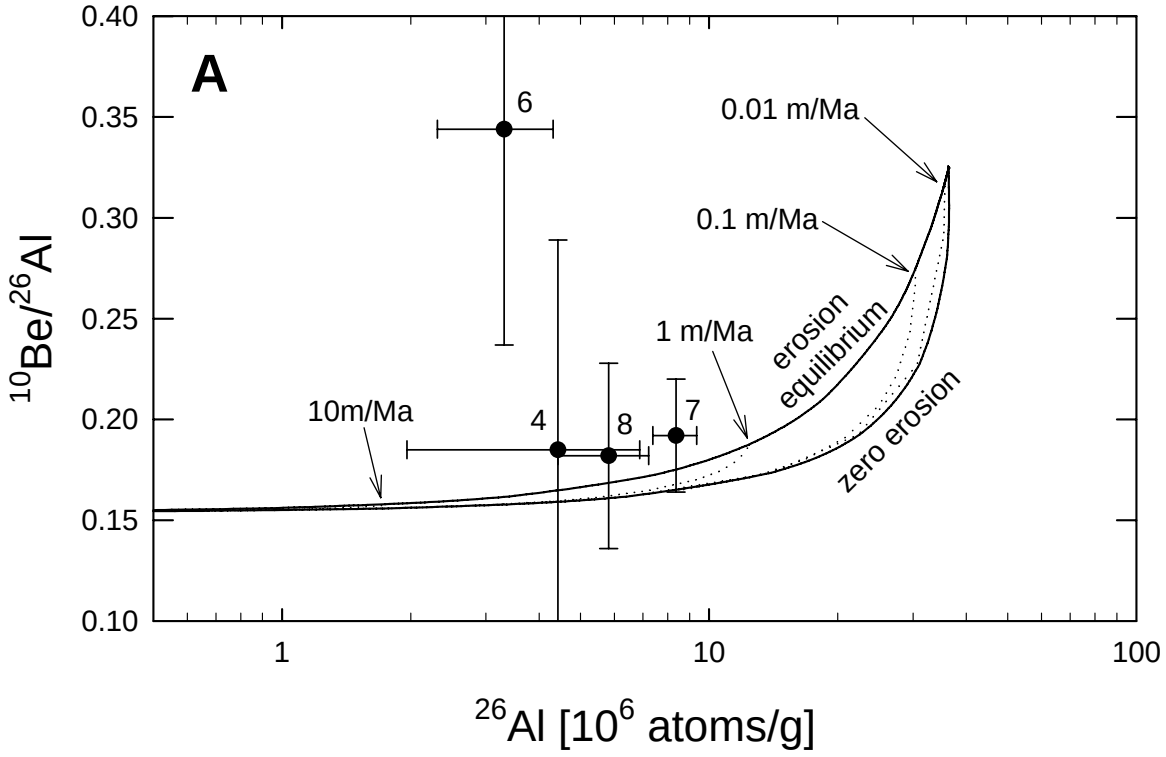
A
0.40
0.35
0.30
0.25
0.20
0.15
0.10
1
10
100
$^{10}Be/^{26}Al$
^{26}Al [10^6 atoms/g]
6
4
8
7
0.01 m/Ma
0.1 m/Ma
1 m/Ma
10m/Ma
erosion equilibrium
zero erosion

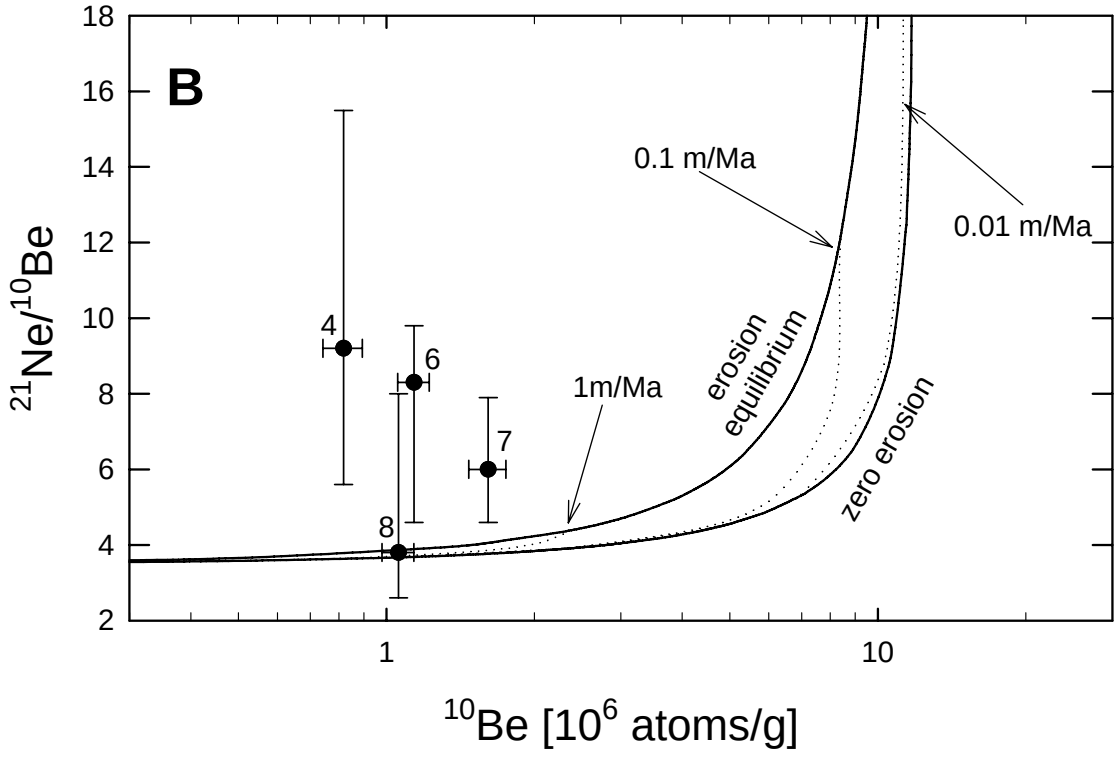
B
18
16
14
12
10
8
6
4
2
1
10
$^{21}Ne/^{10}Be$
^{10}Be [10^6 atoms/g]
4
6
7
8
0.1 m/Ma
0.01 m/Ma
1m/Ma
erosion equilibrium
zero erosion

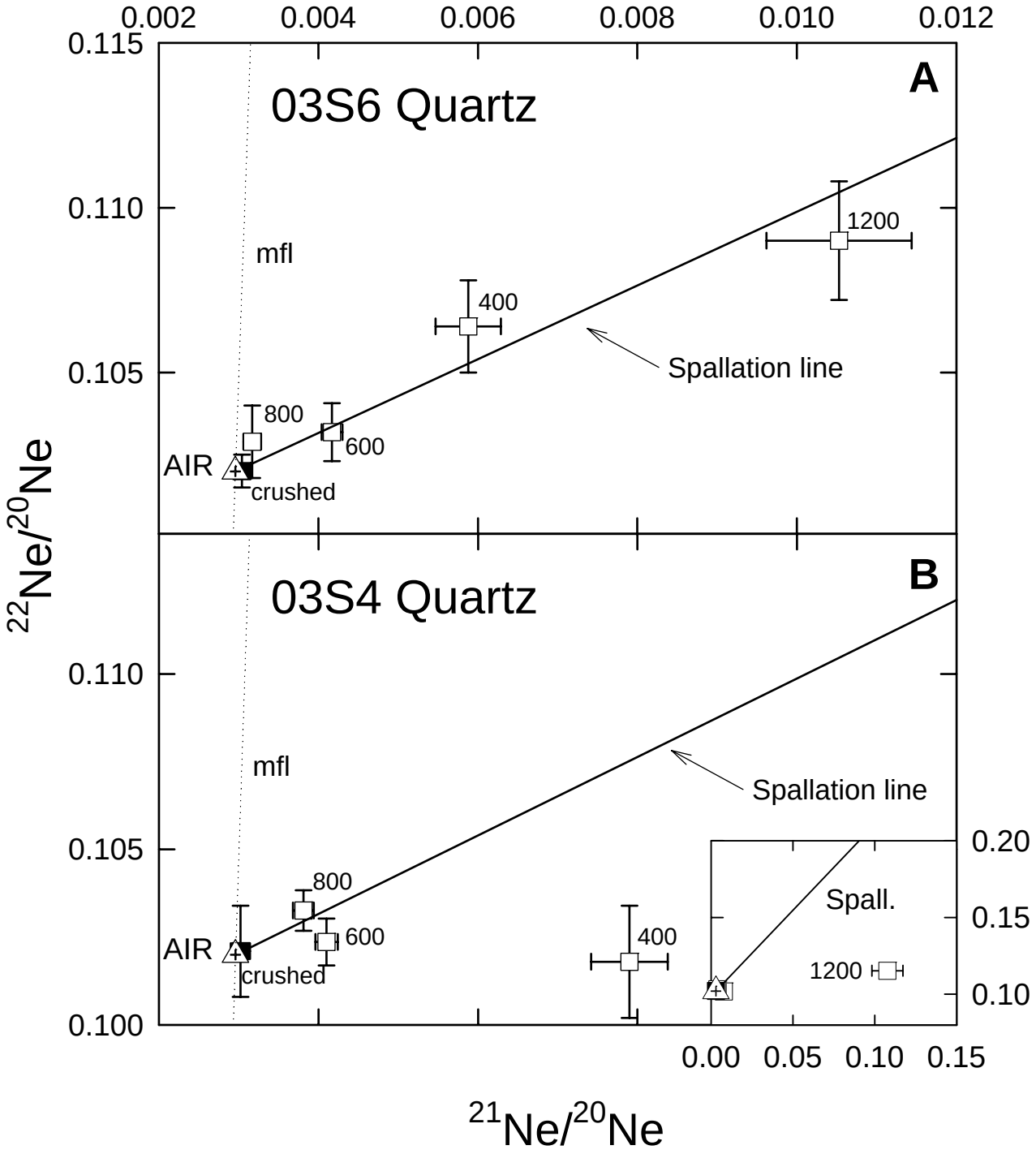
0.002
0.004
0.006
0.008
0.010
0.012
0.115
0.110
0.105
A
03S6 Quartz
mfl
1200
400
Spallation line
800
600
AIR
crushed
B
03S4 Quartz
0.110
0.105
0.100
mfl
Spallation line
800
600
AIR
crushed
400
Spall.
1200
0.20
0.15
0.10
0.00
0.05
0.10
0.15
22Ne/20Ne
21Ne/20Ne

A Progressive widening of a wave-cut platform

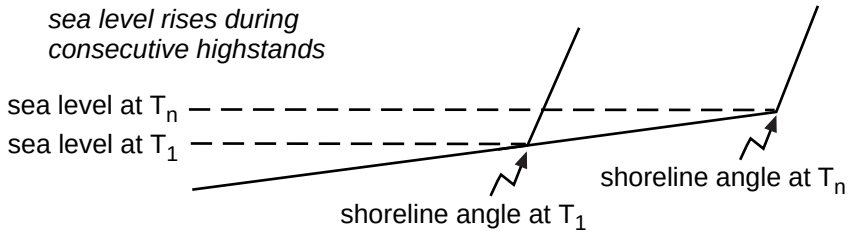

B Emergence of the platform by rock uplift

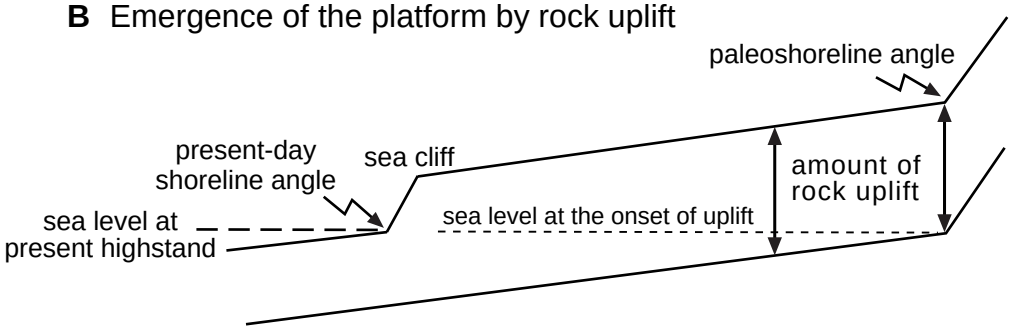

C Preservation of fault offsets after emergence

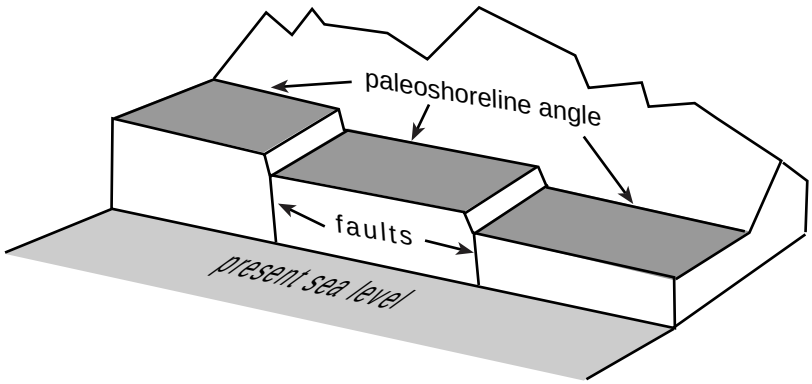

Figure 8 Alvarez-Marron et al.

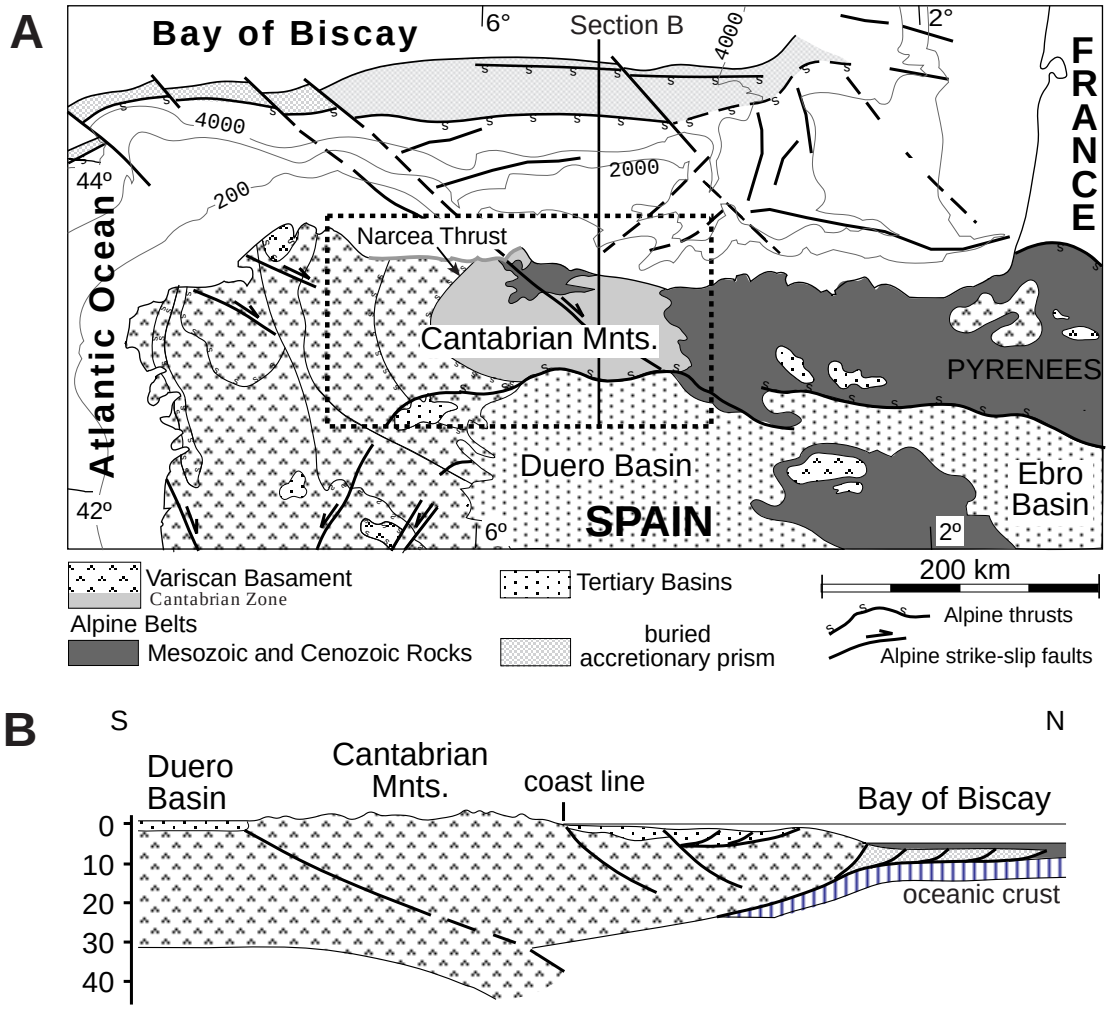

Figure 9. Alvarez-Marron et al.

Table 1. Helium and neon concentrations and neon isotopic compositions in quartz samples from Asturias, as determined by stepwise heating and crushing. Error limits are 2σ.

Sample	T	^{4}He	^{20}Ne	^{22}Ne/^{20}Ne	^{21}Ne/^{20}Ne
	°C	*10^{-8} cm^3 STP/g*	*10^{-12} cm^3 STP/g*	*10^{-2}*	*10^{-2}*
JJ-1-99	<400	0.00209	0.70	9.5	0.27
0.6581 g		±0.00052	±0.25	±2.8	±0.15
	600	11.62	106.4	10.28	0.402
		±0.58	±5.5	±0.14	±0.016
	800	160	312	10.255	0.3437
		±18	±17	±0.071	±0.0076
	1700	119.4	36.8	10.42	1.036
		±6.0	±2.1	±0.14	±0.033
	Total	291	456	10.273	0.4131
		±19	±18	±0.060	±0.0079
JJ-1-99	crushed	1.137	154	10.158	0.2980
1.1994 g		±0.057	±13	±0.059	±0.0084
JJ-2-99	<600	20.3	99.4	10.32	0.466
0.6092 g		±1.0	±5.3	±0.13	±0.014
	<660	32.6	101.1	10.213	0.348
		±1.6	±5.3	±0.053	±0.010
	1200	309	289	10.276	0.3231
		±34	±15	±0.052	±0.0074
	1700	27.2	0.85	15.0	14.3
		±1.4	±0.54	±3.0	±8.6
	Total	389	490	10.280	0.381
		±34	±17	±0.043	±0.022
JJ-2-99	crushed	0.295	205	10.254	0.2951
0.6459 g		±0.021	±12	±0.096	±0.0090
03S4	400	14.7	20.6	10.18	0.790
0.7101 g		±1.0	±1.5	±0.16	±0.048
	600	444	294	10.236	0.410
		±57	±19	±0.067	±0.014
	800	1220	223	10.326	0.381
		±150	±15	±0.058	±0.013
	1200	330	1.41	13.5	26
		±29	±0.76	±1.8	±14
	Total	2010	539	10.280	0.479
		±160	±24	±0.045	±0.052
03S4	crushed	11.55	56.2	10.21	0.302
1.0022 g		±0.84	±4.0	±0.13	±0.012

Table 1 (cont.)

Sample	T *°C*	^{4}He 10^{-8} *cm³/g*	^{20}Ne 10^{-12} *cm³/g*	$^{22}Ne/^{20}Ne$ 10^{-2}	$^{21}Ne/^{20}Ne$ 10^{-2}
03S6	400	0.195	44.3	10.64	0.588
0.7065 g		±0.014	±3.0	±0.14	±0.041
	600	6.67	182	10.319	0.417
		±0.60	±12	±0.088	±0.013
	800	15.7	190	10.29	0.317
		±1.1	±12	±0.11	±0.011
	1200	3.60	2.43	11.39	1.58
		±0.31	±0.66	±0.42	±0.34
	Total	26.2	419	10.346	0.396
		±1.3	±17	±0.065	±0.010
03S6	crushed	2.17	99.1	10.201	0.304
1.0014 g		±0.16	±7.0	±0.050	±0.011
03S7	400	0.253	66.8	10.310	0.368
0.7110 g		±0.018	±4.4	±0.083	±0.016
	600	13.51	476	10.334	0.368
		±0.95	±31	±0.076	±0.011
	800	30.4	722	10.306	0.298
		±2.1	±47	±0.035	±0.010
	1200	11.43	32.2	10.48	0.388
		±0.81	±2.3	±0.17	±0.025
	Total	55.6	1297	10.321	0.330
		±2.4	±57	±0.035	±0.007
03S7	crushed	0.203	252	10.121	0.3019
1.0010 g		±0.015	±18	±0.068	±0.0099
03S8	400	1.74	102.0	10.45	0.387
0.7055 g		±0.12	±7.2	±0.11	±0.012
	600	24.3	306	10.214	0.343
		±1.7	±21	±0.058	±0.011
	800	32.8	205	10.318	0.3042
		±2.3	±14	±0.076	±0.0095
	1200	17.2	10.3	10.95	0.556
		±1.2	±1.1	±0.28	±0.053
	Total	76.0	623	10.299	0.3410
		±3.1	±26	±0.042	±0.0067
03S8	crushed	1.172	60.3	10.015	0.295
1.0016 g		±0.086	±4.0	±0.063	±0.014
For reference:					
	Atmosphere			*10.20*	*0.2959*

Table 2. Derivation of cosmogenic Ne concentrations in quartz samples from Asturias. $^{21}Ne_{ex}$ is the total ^{21}Ne excess, relative to the isotopic composition observed in the crushing extraction. $^{21}Ne_c$ (calc.) is the value obtained for cosmogenic ^{21}Ne by assuming a three-component mixture of trapped Ne, cosmogenic Ne, and nucleogenic ^{21}Ne; it is calculated based on the $^{22}Ne/^{20}Ne$ ratio (equation 35 of Niedermann, 2002). In addition to that, $^{21}Ne_c$ (assumed) takes into account that the amount of cosmogenic ^{21}Ne cannot exceed the total ^{21}Ne excess. Units are 10^6 atoms/g; error limits are 2σ.

Sample #	T [°C]	$^{21}Ne_{ex}$	$^{21}Ne_c$ (calc.)	$^{21}Ne_c$ (assumed)
JJ-1-99	<400	<0.024	<0.37	<0.024
	600	3.03±0.48	$2.05^{+3.59}_{-2.05}$	$2.1^{+1.5}_{-2.1}$
	800	4.01±0.67	$4.13^{+5.34}_{-4.13}$	$4.0^{+0.7}_{-4.0}$
	Total	7.04±0.82		$6.1^{+1.6}_{-4.5}$
JJ-2-99	<600	4.54±0.45	$2.87^{+3.11}_{-2.87}$	$2.9^{+2.1}_{-2.9}$
	<660	1.41±0.28	$0.32^{+1.29}_{-0.32}$	$0.3^{+1.3}_{-0.3}$
	1200	2.11±0.58	5.29±3.63	2.11±0.58
	Total	8.06±0.79		$5.3^{+2.5}_{-3.0}$
03S4	400	2.70±0.34	<0.69	<0.69
	600	8.5±1.6	$2.5^{+4.7}_{-2.5}$	$2.5^{+4.7}_{-2.5}$
	800	4.7±1.1	6.8±3.1	4.7±1.1
	Total	15.9±2.0		$7.2^{+4.9}_{-2.7}$
03S6	400	3.38±0.55	4.69±1.53	3.38±0.55
	600	5.52±0.91	5.21±3.87	$5.2^{+1.2}_{-3.9}$
	800	$0.66^{+0.80}_{-0.66}$	$4.1^{+5.0}_{-4.1}$	$0.66^{+0.80}_{-0.66}$
	Total	9.6±1.3		$9.2^{+1.5}_{-4.0}$
03S7	400	1.18±0.35	1.77±1.34	$1.18^{+0.35}_{-0.75}$
	600	8.4±2.0	15.4±8.8	8.4±2.0
	800	<2.0	18.4±6.2	<2.0
	Total	$9.6^{+2.9}_{-2.0}$		$9.6^{+2.9}_{-2.1}$
03S8	400	2.52±0.54	6.1±2.7	2.52±0.54
	600	3.9±1.5	$1.0^{+4.3}_{-1.0}$	$1.0^{+4.3}_{-1.0}$
	800	$0.51^{+0.93}_{-0.51}$	5.8±3.8	$0.51^{+0.93}_{-0.51}$
	Total	$6.9^{+1.8}_{-1.7}$		$4.0^{+4.4}_{-1.2}$

Table 3: ^{21}Ne, ^{10}Be and ^{26}Al minimum ages of samples from the marine terrace, Asturias, Spain.

Sample ID	Location N W	Alti-tude (m)	^{21}Ne* (10^6 at/g)	Error**	Prod. rate # (at/g/a)	^{21}Ne age (ka) §	Error **	^{10}Be (10^6 at/g)	Prod. rate # (at/g/a)	^{10}Be age (ka) §	^{26}Al (10^6 at/g)	Prod. rate # (at/g/a)	^{26}Al age (ka) §
03S4	43°33.36' 6°35.99'	70	7.2	+4.9 -2.7	18.3	390	+270 -150	0.786±0.072	5.21	156±15	4.2±2.4	33.8	134±79
03S6	43°35.48' 6°14.40'	90	9.2	+1.5 -0.40	18.6	500	+80 -220	1.115±0.082	5.31	221±17	3.24±0.98	34.5	98±31
03S7	43°35.06' 6°01.79'	100	9.6	+2.9 -2.1	18.8	510	+150 -110	1.59±0.13	5.36	319±29	8.27±0.98	34.8	270±37
03S8	43°39.34' 5°51.39'	100	4.0	+4.4 -1.2	18.8	210	+230 -60	1.046±0.078	5.36	204±16	5.8±1.4	34.8	180±48
JJ-1-99	43°39.15' 5°51.16'	100	6.1	+1.6 -4.5	18.8	320	+90 -240	–	–	–	–	–	–
JJ-2-99	43°35.07' 6°01.78'	100	5.3	+2.5 -3.0	18.8	280	+130 -160	–	–	–	–	–	–

***** The cosmogenic ^{21}Ne concentration has been obtained by correcting the measured ^{21}Ne concentration for nucleogenic neon.

** All errors are reported at the 95% confidence level.

Production rates used for calculation of the minimum ages have been scaled to the latitude and altitude of the sampling sites using the scaling procedure of Dunai [27].

§ All nominal ages have been calculated assuming no erosion and continuous exposure, which means that the ages are only minimum ages. The error limits of the exposure ages do not include the uncertainties of the production rates and the scaling method.

Table 4: Concentrations of ^{21}Ne, ^{10}Be, ^{26}Al, and paired-nuclide interpretation for ^{21}Ne – ^{10}Be and ^{10}Be – ^{26}Al of bedrock samples from the marine terrace, Asturias, Spain. The minimum total time since initial exposure is obtained by summing the minimum exposure and the minimum burial time. The given error limits (95% confidence level) have been analytically derived using common error propagation for ^{21}Ne-^{10}Be, but are only estimates for ^{10}Be-^{26}Al (see text).

Sample ID	^{21}Ne (10^6 at/g)	^{10}Be (10^6 at/g)	^{26}Al (10^6 at/g)	Paired nuclide interpretation ^{21}Ne – ^{10}Be			Paired nuclide interpretation ^{10}Be – ^{26}Al		
				minimum exposure (ka)	minimum burial (ka)	minimum total (ka)	minimum exposure (ka)	minimum burial (ka)	minimum total (ka)
03S4	7.2 +4.9/-2.7	0.786 ±0.072	4.2 ±2.4	390 +270/-150	1900 +1400/-800	**2290** +1600/-900	180 +220/-40	270 +1500/-270	450 +1700/-310
03S6	9.2 +1.5/-4.0	1.115 ±0.082	3.24 ±0.98	490 +80/-220	1630 +360/-860	**2120** +430/-1070	430 +200/-110	1350 +670/-530	1780 +850/-600
03S7	9.6 +2.9/-2.1	1.59 ±0.13	8.27 ±0.98	510 +150/-110	930 +610/-460	**1440** +760/-560	360 +70/-50	250 +280/-220	610 +330/-250
03S8	4.0 +4.4/-1.2	1.046 ±0.078	5.8 ±1.4	210 +230/-20	90 +2300/-90	**300** +2500/-110	230 +80/-40	210 +550/-210	440 +600/-250